Repeat-Pass Synthetic Aperture Sonar Micro-Navigation using Redundant Phase Center Arrays

Alan J. Hunter, *Member, IEEE,* Samantha Dugelay, and Warren L. J. Fox

Abstract

A new algorithm is introduced for high-precision underwater navigation using the coherent echo signals collected during repeat-pass synthetic aperture sonar (SAS) surveys. The algorithm is a generalization of redundant phase center (RPC) micro-navigation, expanded to redundant phase centers formed between overlapping pings in repeated passes. For each set of overlapping ping pairs (two intra-pass and three inter-pass), five different RPC arrays can be formed to provide estimates of the vehicle's surge, sway, and yaw. These estimates are used to find a weighted least-squares solution for the trajectories of the repeated passes. The algorithm can estimate the relative trajectories to sub-wavelength precision (on order of millimeters to 100s of microns at typical SAS operating frequencies of 100s of kHz) in a common coordinate frame. This will lead to improved focusing and co-registration for repeat-pass SAS interferometry and is an important step towards repeat-pass bathymetric mapping. The repeat-pass RPC micro-navigation algorithm is demonstrated using data collected by the 300 kHz SAS of the NATO Center for Maritime Research and Experimentation (CMRE) Minehunting Unmanned underwater vehicle for Shallow water Covert Littoral Expeditions (MUSCLE).

Index Terms

Synthetic aperture sonar, micro-navigation, repeat-pass interferometry, coherent change detection

I. Introduction

Synthetic aperture sonar (SAS) images are generated by coherently processing the signals collected along a synthetic array, which is formed as the sonar platform traverses its path through the water. SAS provides very high-resolution imagery of the seafloor that is independent of both range and frequency [1]. However, sub-wavelength navigation precision is required to support this coherent processing (i.e., an order of magnitude less than the

A. Hunter is with the University of Bath, Claverton Down Rd, Bath BA2 7AY, North East Somerset, United Kingdom; e-mail: a.j.hunter@bath.ac.uk.

S. Dugelay is with the NATO Science and Technology Organization, Center for Maritime Research and Experimentation, Viale San Bartolomeo 400, 19126 La Spezia, Italy.

W. Fox is with the Applied Physics Lab, University of Washington, 1013 NE 40th St, Seattle, WA 98105, USA.

wavelength [2][3, chapter 5]). The consequence of failing to meet this requirement is the introduction of image errors, including defocusing and image artefacts [4]. For SAS systems operating at frequencies of 100s of kHz, the requirement equates to precision on the order of millimeters to 100s of microns. This is challenging, but it can be achieved using a combination of navigation hardware on the sonar platform and data-driven micro-navigation algorithms.

Micro-navigation algorithms provide "through-the-sensor" navigation estimates using the sonar echo signals. For the translational motions of sway and surge (across-track and along-track), which contribute strongly to imaging errors, micro-navigation provides much better precision than integrated velocity measurements from an inertial navigation system (INS) and Doppler velocity log (DVL) [5], [6]. The other motion which contributes most to SAS imaging errors is yaw (rotation in the imaging plane) and this can be measured adequately using high-end INSs with sufficiently low drift rates. SAS is relatively insensitive to variations in heave, pitch, and roll.

The most popular approach to SAS micro-navigation is the redundant phase center (RPC) algorithm, also commonly referred to as the displaced phase center antenna (DPCA) algorithm [7], [8]. RPC micro-navigation operates by forming a virtual array from the cross-correlation of signals between redundant phase center arrays – that is, the overlapping (redundant) portion of the sonar array at subsequent pings. The ping-to-ping sway and surge are estimated by beamforming this virtual array and locating the peak in the correlation function. Furthermore, the amplitude of the peak is related to the signal-to-noise ratio and can be used to approximate the estimation error [9], [10].

Coherent processing of signals from repeated passes over the same scene opens up a range of new capabilities for SAS. These include coherent change detection [11] and repeat-pass interferometric bathymetry estimation. Although interferometric SAS [12] and repeat-pass interferometric synthetic aperture radar [13] are widely used, repeat-pass interferometric SAS is still in its infancy. Coherent repeat-pass processing adds further challenges to the navigation problem since navigation errors can accumulate substantially between passes and temporal and angular changes can act to reduce signal coherence. Coherent image registration from repeated passes has been approached successfully using feature matching methods, such as the scale invariant feature transform (SIFT), e.g., [14], [15], [16], [17]. Others have demonstrated repeat-pass co-registration at the signal level, and investigated the effect of the correlation coefficient on across-track separation and element size [18].

In this paper, we present a new SAS micro-navigation algorithm for coherent repeat-pass data registration at the signal level. The algorithm is a generalization of the RPC algorithm and is detailed in Section II. It is demonstrated in Section III using data collected by the 300 kHz SAS of the MUSCLE autonomous underwater vehicle during the Multi-national AutoNomy EXperiment, 2014 (MANEX 14) sea trial. We use the algorithm to generate repeat-pass coherence and interferometric phase maps of the seafloor. These results show the feasibility of coherent change detection and interferometric processing at 300 kHz over time scales of at least tens of minutes in the area of the Ligurian Sea where the experiments were conducted. They also indicate the potential and some challenges for applications of repeat-pass interferometry, which are discussed in Section IV.

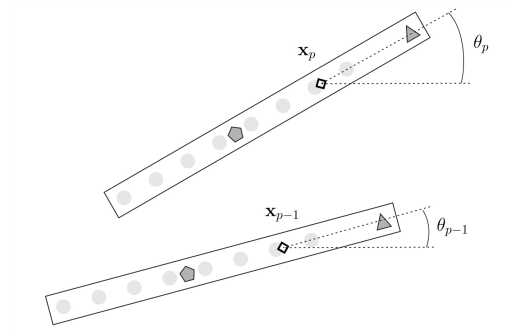

(a)

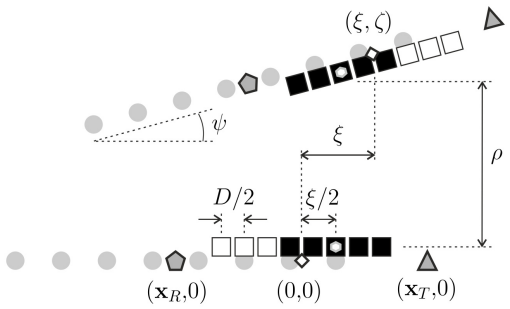

(b)

Fig. 1. Geometry for the redundant phase center micro-navigation algorithm: (a) estimation of surge and sway $\mathbf{x}_p$ and yaw θ_p by accumulation of ping-to-ping rate estimates; (b) estimation of ping-to-ping surge rate ξ, sway rate ζ, and yaw rate ψ. The various symbols represent the following: triangle – projector; circle – hydrophone; pentagon – center of hydrophone array; square – phase center; black square – redundant phase center; diamond – center of phase center array; hexagon – center of redundant phase center array.

II. Repeat-Pass Micro-Navigation Algorithm

The single-pass RPC algorithm is first recapped in Section II-A to introduce our mathematical notation. This is based mostly on [19], which provides a very thorough description of the algorithm and its implementation details. The repeat-pass generalization, which is the main novel contribution of this work, is then introduced in Section II-B and Section II-C. The algorithm operates on the aligned ping pairs from each pass; there are several ways to perform this alignment and these are discussed in Section II-D.

A. Redundant Phase-Center (RPC) Micro-Navigation

Consider a sonar system comprising a single projector and a linear array of N equally-spaced hydrophones. In the far-field, the phase center approximation can be employed to replace these bistatic pairs with an array of N virtual monostatic pairs located at the midpoints (phase centers) between the physical source and each physical hydrophone. The local position of the nth phase center is given by

$$u_n = \left(n - \frac{N-1}{2}\right)\Delta u, \qquad n \in [0, N-1] \tag{1}$$

relative to the middle of the array, where $\Delta u = D/2$ is the phase center spacing and D is the hydrophone spacing. When the along-track ping-to-ping displacements are small enough, a portion of the phase centers from subsequent pings will overlap, as illustrated in Figure 1b. These are termed "redundant phase centers" since their signals contain redundant information on the scene reflectivity. The RPC algorithm exploits these redundant signals to obtain a precise estimation of the sonar path. The algorithm operates as follows.

Assume that some redundant phase centers are formed between adjacent ping pairs denoted by the indices $p-1$ and p. We term these overlapping portions of the sonar phase center array the redundant phase center array or RPC array. The RPC array is one of a collection of possible candidates that can be formed by assuming along-track displacements in integer multiples of the phase center spacing

$$u'_m = m\Delta u, \qquad m \in [-(N-1), N-1]\,. \tag{2}$$

There are $2N-1$ possible candidates. However, typically, the nominal value $m_0 = v/f_p/\Delta u$ is known from the speed of the sonar platform v and the ping rate f_p.

For each candidate RPC array, the signals from all overlapping phase centers are cross-correlated over a time window corresponding to an interval of slant ranges. This results in a correlation function over the 3-D domain of: correlation delays t', along-track displacements u'_m used to form the candidate arrays, and positions of the overlapping phase centers in the candidate array

$$\eta_{l,m} = \left(l - \frac{N-1}{2} - \frac{|m|}{2}\right)\Delta u, \qquad l \in \left[0, N-1-\left|m\right|\right]. \tag{3}$$

Note that these positions are expressed in a coordinate system local to the center of the candidate array and that the support of the correlation function over η decreases with the number of non-overlapping phase centers.The correlation function is given by

$$\gamma_{p-1,p}\left(t', u'_m, \eta_{l,m}\right) = \int_{\frac{2r}{c}-\frac{R}{c}}^{\frac{2r}{c}+\frac{R}{c}} d^*_{p-1}\left(t, u_{n_0}\right)\; d_p\left(t+t', u_{n_1}\right)\; \mathrm{d}t, \tag{4}$$

where $d_q\left(t, u_n\right)$ are the matched-filtered signals from the sonar array at the qth ping, t is time, and

$$n_0 = \begin{cases} l+m & m \geq 0 \\ l, & m < 0 \end{cases} \tag{5}$$

and

$$n_1 = \begin{cases} l & m \geq 0 \\ l-m, & m < 0 \end{cases} \tag{6}$$

are the indices of the sonar array elements evaluated in the qth and $(q+1)$th ping. The correlation window is centered on the slant range r with an interval of R and $c \approx 1500\ \mathrm{m/s}$ is the acoustic propagation speed.

The cross-correlation signals from each candidate array are then beamsteered over a range of angles ϕ and a search is made for the peak in the coherence, i.e.,

$$\left(t'', \xi, \psi\right) = \underset{t', u'_m, \phi}{\arg\max} \left\{ \left|\Gamma_{p-1,p}\left(t', u'_m, \phi\right)\right| \right\}, \tag{7}$$

where

$$\Gamma_{p-1,p}\left(t', u'_m, \phi\right) = \sum_{l=0}^{N-1-|m|} \gamma_{p-1,p}\left(t', u'_m, \eta_{l,m}\right) \exp\left(jk_c \sin\left(\phi\right) \eta_{l,m}\right), \tag{8}$$

and $k_c = 2\pi f_c / c$ is the wavenumber at the center frequency f_c.

This yields relative ping-to-ping estimates in the slant range plane for the lateral displacement (surge rate) ξ in $\mathrm{m/ping}$ and rotation (yaw rate) ψ in $\mathrm{deg/ping}$ of the phase center array, and a coarse estimate of the time-delay t'' induced by the transverse displacement of the RPC array. The correlation function (8) is coarsely sampled in u' at multiples of the phase center spacing $D/2$. Therefore, it is common practice to perform an interpolation (e.g., [20], [21], [19]) to achieve surge rate estimates with sub-element precision. The coarse estimate t'' is also refined using the phase at the peak coherence to provide sub-wavelength precision, i.e.,

$$\tau = \left(-\frac{\alpha}{2\pi} + M\right) \frac{1}{fc}, \tag{9}$$

where

$$\alpha = \angle\, \Gamma_{p-1,p}\left(t'', \xi, \psi\right) \tag{10}$$

is the phase at the peak and M is the number of wrapped wavelengths in the coarse time delay. The transverse displacement of the RPC array (RPC sway rate) is then given by $\rho = \tau c/2$ and the transverse displacement of the phase center array (sway rate) ξ can be computed from the RPC sway rate using

$$\zeta = \rho + \frac{\xi}{2} \sin\left(\psi\right), \tag{11}$$

where $\xi/2$ is the offset of the RPC array with respect to the phase center array. The geometry is illustrated in Figure 1b.

There are several methods for solving (7) to find the peak. Also, care must be taken to ensure that the phase is unwrapped correctly in (9). These implementation details are not discussed here, but a good summary can be found in [19].

Finally, the total path (expressed in the slant-range plane for the range r) can be estimated by accumulating the yaw, surge, and sway rates relative to an assumed initial heading θ_0 and position $\mathbf{x}_0$ (e.g., $\mathbf{x}_0 = \mathbf{0}$ and $\theta_0 = 0$). The heading at the $p\mathrm{th}$ ping is given by

$$\theta_p = \theta_0 + \sum_{q=1}^{p} \Delta\theta_{q-1,q}, \tag{12}$$

where

$$\Delta\theta_{p-1,p} = \psi. \tag{13}$$

The path position is given by

$$\mathbf{x}_p = \mathbf{x}_0 + \sum_{q=1}^{p} \Delta\mathbf{x}_{q-1,q}, \tag{14}$$

where

$$\Delta\mathbf{x}_{p-1,p} = \begin{pmatrix} \cos\theta_{p-1} & -\sin\theta_{p-1} \\ \sin\theta_{p-1} & \cos\theta_{p-1} \end{pmatrix} \begin{pmatrix} \xi \\ \zeta \end{pmatrix}. \tag{15}$$

The geometry is illustrated in Figure 1a.

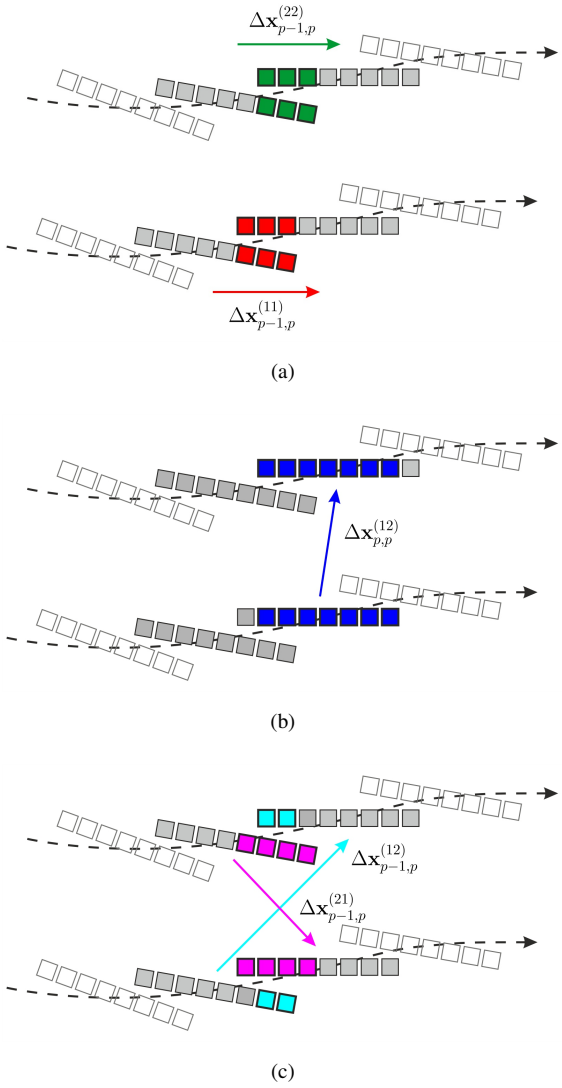

Fig. 2. Repeat-pass redundant phase center arrays: conventional RPC arrays within the same pass (red and green) and RPC arrays between passes (blue, cyan, and magenta).

B. Repeat-Pass RPC Micro-Navigation

Consider now two separate passes over the same scene at different times. Naturally, it is possible to perform conventional RPC micro-navigation for each of these passes independently, as described above. We denote the individual passes using the superscripts $\cdot^{(11)}$ and $\cdot^{(22)}$ for the first and second pass, respectively. The corresponding micro-navigation estimates are then denoted

$$\Delta\mathbf{x}_{p-1,p}^{(11)}, \Delta\theta_{p-1,p}^{(11)} \tag{16}$$

and

$$\Delta\mathbf{x}_{p-1,p}^{(22)}, \Delta\theta_{p-1,p}^{(22)}. \tag{17}$$

However, in addition to these *intra*-pass estimates, it is possible to also obtain *inter*-pass estimates using RPC arrays formed between the passes. We denote these estimates using the superscripts $\cdot^{(12)}$ and $\cdot^{(21)}$ for estimates from the first to the second pass and vice versa, respectively. Assuming, as before, that only adjacent ping pairs have redundant phase centers, three additional RPC arrays can be formed between the passes, yielding the estimates:

$$\Delta\mathbf{x}_{p,p}^{(12)}, \Delta\theta_{p,p}^{(12)} \tag{18}$$

$$\Delta\mathbf{x}_{p-1,p}^{(12)}, \Delta\theta_{p-1,p}^{(12)} \tag{19}$$

and

$$\Delta\mathbf{x}_{p-1,p}^{(21)}, \Delta\theta_{p-1,p}^{(21)}. \tag{20}$$

The total of five RPC arrays are illustrated in Figure 2. It is straightforward to generalize to the case of more than two overlapping phase center arrays and also to more than two passes.

We wish to estimate the relative trajectories $\mathbf{x}_p^{(1)}$, $\theta_p^{(1)}$ and $\mathbf{x}_p^{(2)}$, $\theta_p^{(2)}$ of the two passes for all $p \in [0, P-1]$, with respect to a common reference position and heading (e.g., $\mathbf{x}_0^{(1)} = \mathbf{0}$ and $\theta_0^{(1)} = 0$). This can be achieved by solving the system of linear equations relating the intra and inter-pass RPC estimates of surge and sway and the estimates or INS measurements of yaw, (16) – (20). In practice, measurements from the INS/DVL provide a useful independent source of information and should also be utilized. This can be done by incorporating the measurements into the system of equations or, as is common in most implementations of the conventional RPC algorithm, by fusion through a Kalman filter [22].

C. Weighted Least-Squares Solution

The relative heading estimates $\hat{\theta}_p^{(1)}$ and $\hat{\theta}_p^{(2)}$ can be made independently of the other (translational) dimensions since the yaw is invariant with surge and sway. Therefore, these should be computed first.

The measured yaw rates $\Delta\theta_{a,b}^{(ij)}$ can be expressed from the unknown headings $\theta_c^{(k)}$ via the following system of equations:

$$\mathbf{A}\boldsymbol{\Theta} = \Delta\boldsymbol{\Theta}, \tag{21}$$

where

$$\boldsymbol{\Theta} = \left(\begin{array}{c|c|c|c} \theta_0^{(1)} \; \theta_0^{(2)} & \theta_1^{(1)} \; \theta_1^{(2)} & \cdots & \theta_{P-2}^{(1)} \; \theta_{P-2}^{(2)} \; \theta_{P-1}^{(1)} \; \theta_{P-1}^{(2)} \end{array} \right)^{\mathrm{T}} \tag{22}$$

is a $2P \times 1$ vector of the unknown headings at each ping from each pass,

$$\begin{aligned} \Delta\boldsymbol{\Theta} = \Big(\; 0 \; \Delta\theta_{0,0}^{(12)} \; \big| \; & \Delta\theta_{0,1}^{(11)} \; \Delta\theta_{0,1}^{(22)} \; \Delta\theta_{1,1}^{(12)} \; \Delta\theta_{0,1}^{(12)} \; \Delta\theta_{0,1}^{(21)} \; \big| \\ & \cdots \; \big| \; \Delta\theta_{P-2,P-1}^{(11)} \; \Delta\theta_{P-2,P-1}^{(22)} \; \Delta\theta_{P-1,P-1}^{(12)} \; \Delta\theta_{P-2,P-1}^{(12)} \; \Delta\theta_{P-2,P-1}^{(21)} \; \Big)^{\mathrm{T}} \end{aligned} \tag{23}$$

is a $(5P-3)\times 1$ vector of the intra and inter-pass yaw estimates, and

$$\mathbf{A}=\begin{pmatrix}
\begin{bmatrix}1&0\\-1&1\end{bmatrix} & \mathbf{0} & \mathbf{0} & \dots & \mathbf{0} & \mathbf{0}\\
\begin{bmatrix}-1&0&1&0\\0&-1&0&1\\0&0&-1&1\\-1&0&0&1\\0&1&-1&0\end{bmatrix} & & \mathbf{0} & \dots & \mathbf{0} & \mathbf{0}\\
\mathbf{0} & \begin{bmatrix}-1&0&1&0\\0&-1&0&1\\0&0&-1&1\\-1&0&0&1\\0&1&-1&0\end{bmatrix} & & \dots & \mathbf{0} & \mathbf{0}\\
 & & & \ddots & & \\
\mathbf{0} & \mathbf{0} & \mathbf{0} & \dots & \begin{bmatrix}-1&0&1&0\\0&-1&0&1\\0&0&-1&1\\-1&0&0&1\\0&1&-1&0\end{bmatrix} &
\end{pmatrix} \tag{24}$$

is a $(5P-3)\times 2P$ matrix.

The system of equations (21) is overdetermined. Furthermore, each equation can be weighted according to an infinite time-series approximation [23] for the effective signal-to-noise ratio

$$\mathrm{SNR}\approx\frac{\Gamma}{1-\Gamma} \tag{25}$$

since this is directly proportional to the variance of the estimation error [10]. Thus, a weighted least-squares solution can be found for the headings, i.e.,

$$\hat{\boldsymbol{\Theta}}=\left(\mathbf{W}^{1/2}\mathbf{A}\right)^{+}\mathbf{W}^{1/2}\Delta\boldsymbol{\Theta} \tag{26}$$

where $\left(\mathbf{W}^{1/2}\mathbf{A}\right)^{+}\mathbf{W}^{1/2}$ is the weighted pseudo-inverse of $\mathbf{A}$, the superscript + denotes the Moore-Penrose pseudo-inverse [24], i.e.,

$$\mathbf{B}^{+}=\left(\mathbf{B}^{\mathrm{T}}\mathbf{B}\right)^{-1}\mathbf{B}^{\mathrm{T}}, \tag{27}$$

$\mathbf{W}$ is a $(5P-3)\times(5P-3)$ matrix of weights with nonzero elements on the diagonal only given by

$$\begin{aligned}\mathrm{diag}\left\{\mathbf{W}\right\}=\Big(\ \infty\ \mathrm{SNR}_{0,0}^{(12)}\ \big|\ &\mathrm{SNR}_{0,1}^{(11)}\ \mathrm{SNR}_{0,1}^{(22)}\ \mathrm{SNR}_{1,1}^{(12)}\ \mathrm{SNR}_{0,1}^{(12)}\ \mathrm{SNR}_{0,1}^{(21)}\ \big|\\ &\dots\ \big|\ \mathrm{SNR}_{P-2,P-1}^{(11)}\ \mathrm{SNR}_{P-2,P-1}^{(22)}\ \mathrm{SNR}_{P-1,P-1}^{(12)}\ \mathrm{SNR}_{P-2,P-1}^{(12)}\ \mathrm{SNR}_{P-2,P-1}^{(21)}\ \Big)^{\mathrm{T}}\end{aligned} \tag{28}$$

Fig. 3. The MUSCLE autonomous underwater vehicle of the NATO Centre for Maritime Research and Experimentation.

The first term in (28) is infinite because it corresponds to the prescribed reference position and orientation for the first ping of the first pass. In practice, an infinite value causes implementation issues and it is necessary to use a large finite value (e.g., 100 dB) instead.

After solving for the headings, the surge and sway estimates must be updated to reflect the difference between the independent coordinate frames of each individual pass and the new common coordinate frame of both passes. The updated displacement vectors are given by

$$\Delta\mathbf{x}_{a,b}^{\prime(ij)} = \begin{pmatrix} \cos\theta_a^{\prime(i)} & -\sin\theta_a^{\prime(i)} \\ \sin\theta_a^{\prime(i)} & \cos\theta_a^{\prime(i)} \end{pmatrix} \Delta\mathbf{x}_{a,b}^{(ij)}, \tag{29}$$

where

$$\theta_a^{\prime(i)} = \hat{\theta}_a^{(i)} - \theta_a^{(i)} \tag{30}$$

is the change in heading between the independent and common frames. A similar system of equations can then be established to relate the displacements to the path positions:

$$\mathbf{A}\mathbf{X} = \Delta\mathbf{X}, \tag{31}$$

where

$$\mathbf{X} = \left(\begin{array}{c|c|c|c|c} \mathbf{x}_0^{(1)}\ \mathbf{x}_0^{(2)} & \mathbf{x}_1^{(1)}\ \mathbf{x}_1^{(2)} & \cdots & \mathbf{x}_{P-2}^{(1)}\ \mathbf{x}_{P-2}^{(2)} & \mathbf{x}_{P-1}^{(1)}\ \mathbf{x}_{P-1}^{(2)} \end{array} \right)^{\mathrm{T}} \tag{32}$$

is a $2P \times 1$ vector of the unknown 2-D positions at each ping from each pass, and

$$\begin{aligned} \Delta\mathbf{X} = \Big(\; 0\ \Delta\mathbf{x}_{0,0}^{(12)} \;\Big|\; & \Delta\mathbf{x}_{0,1}^{(11)}\ \Delta\mathbf{x}_{0,1}^{(22)}\ \Delta\mathbf{x}_{1,1}^{(12)}\ \Delta\mathbf{x}_{0,1}^{(12)}\ \Delta\mathbf{x}_{0,1}^{(21)} \;\Big| \\ & \cdots \;\Big|\; \Delta\mathbf{x}_{P-2,P-1}^{(11)}\ \Delta\mathbf{x}_{P-2,P-1}^{(22)}\ \Delta\mathbf{x}_{P-1,P-1}^{(12)}\ \Delta\mathbf{x}_{P-2,P-1}^{(12)}\ \Delta\mathbf{x}_{P-2,P-1}^{(21)} \; \Big)^{\mathrm{T}} \end{aligned} \tag{33}$$

is a $(5P-3) \times 1$ vector of the updated intra and inter-pass 2-D displacements. The system of equations can be solved in the same way as before to provide estimates of the path positions, i.e.,

$$\hat{\mathbf{X}} = \left(\mathbf{W}^{1/2}\mathbf{A}\right)^{+} \mathbf{W}^{1/2}\Delta\mathbf{X}. \tag{34}$$

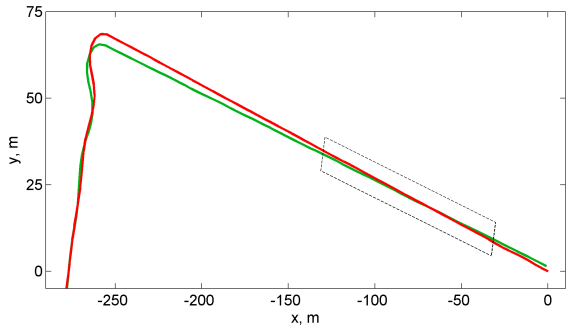

Fig. 4. Tracks of repeated passes with a 1 deg heading difference made by the MUSCLE AUV during the MANEX '14 trial. The boxed region indicates the interval of 256 pings centered roughly on the crossing point, which was used to demonstrate the repeat-pass micro-navigation algorithm.

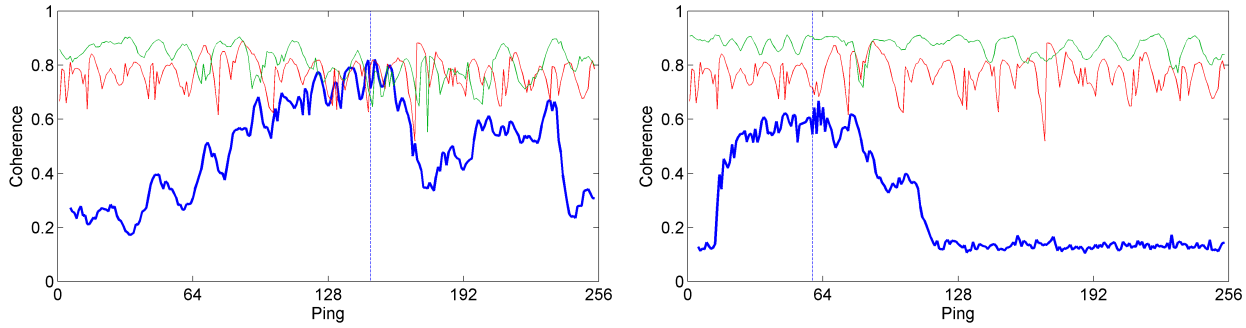

(a) (b)

Fig. 5. Coherence values from conventional RPC micro-navigation on the first (red) and second (green) passes and repeat-pass RPC micro-navigation between passes (blue) for (a) a 1 deg heading difference between passes and (b) a 2 deg difference. The vertical dotted lines indicate the pings corresponding to the crossing paths (i.e., zero inter-pass sway).

D. Alignment of ping pairs in repeated passes

The repeat-pass RPC micro-navigation algorithm presented in Sections II-B to II-C assumes that the pings from each pass are aligned. That is, that the corresponding pings denoted by the index p have maximally overlapping phase centers. In practice, they will not be aligned in this way and the alignment must be carried out in a pre-processing stage. Expressing the ping indices of the first pass as $p_1 = p$ and the misaligned second pass as $p_2 = p + \Delta p\,(p)$, the goal is to find the inter-pass ping offset as a function of ping index $\Delta p\,(p)$. A method for aligning pings from repeated passes has already been proposed elsewhere [18] in addition to an associated method for estimating the bulk inter-pass navigation error. We use a similar approach.

To limit the computational burden, we assume that the ping offset varies slowly with the ping index. Therefore, it can be estimated using only a limited sub-set of pings and nearest-neighbor interpolation of the results. For each sample ping $p' \in [0, P-1]$ from the first pass, RPC array candidates are formed with all pings from the second pass that are within a limited search range $p' + q$, where $q \in [-Q/2, Q/2]$; the search range Q can be selected

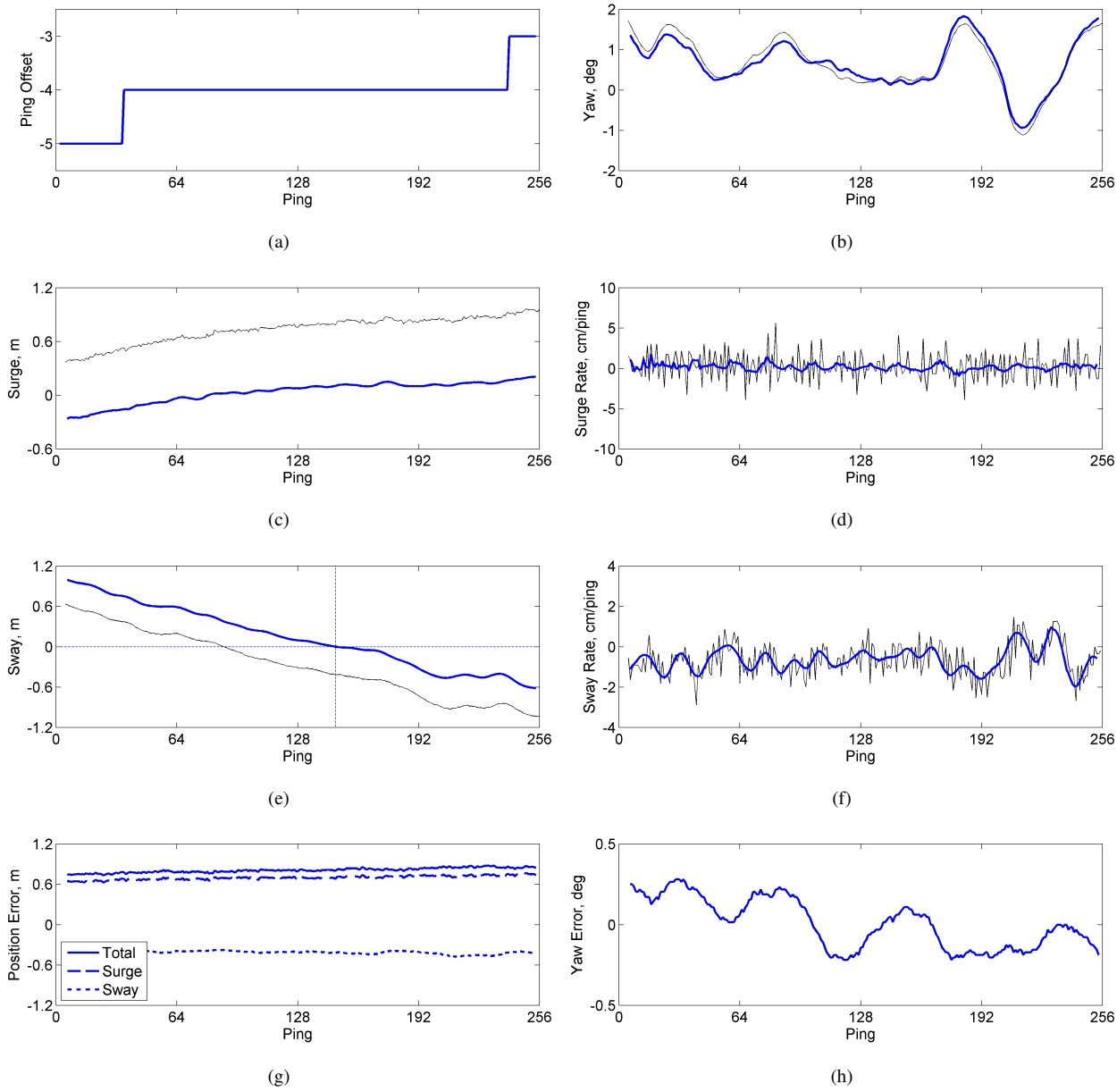

Fig. 6. Comparison of the inter-pass surge, sway, and yaw for repeated passes with a 1 deg heading difference, as estimated by repeat-pass RPC micro-navigation (blue) and measured by the navigation hardware (black): (a) ping offset; (b) yaw; (c,d) surge and surge rate; (e,f) sway and sway rate; and (g,h) errors in the position and yaw measurements relative to the micro-navigation estimates. The dotted lines in (e) indicate the ping corresponding to the crossing paths.

based on the maximum expected navigation error between passes. A search is then made for the RPC array with maximum coherence, thus yielding the ping offset, i.e.,

$$\left(t'', \xi, \psi, \Delta p\left(p'\right)\right) = \underset{t', u', \phi, q}{\arg\max} \left\{ \left| \Gamma^{(12)}_{p', p'+q}\left(t', u', \phi\right) \right| \right\}, \tag{35}$$

where the correlation function Γ is defined by (8) and the superscript $\cdot^{(12)}$ denotes the inter-pass correlation.

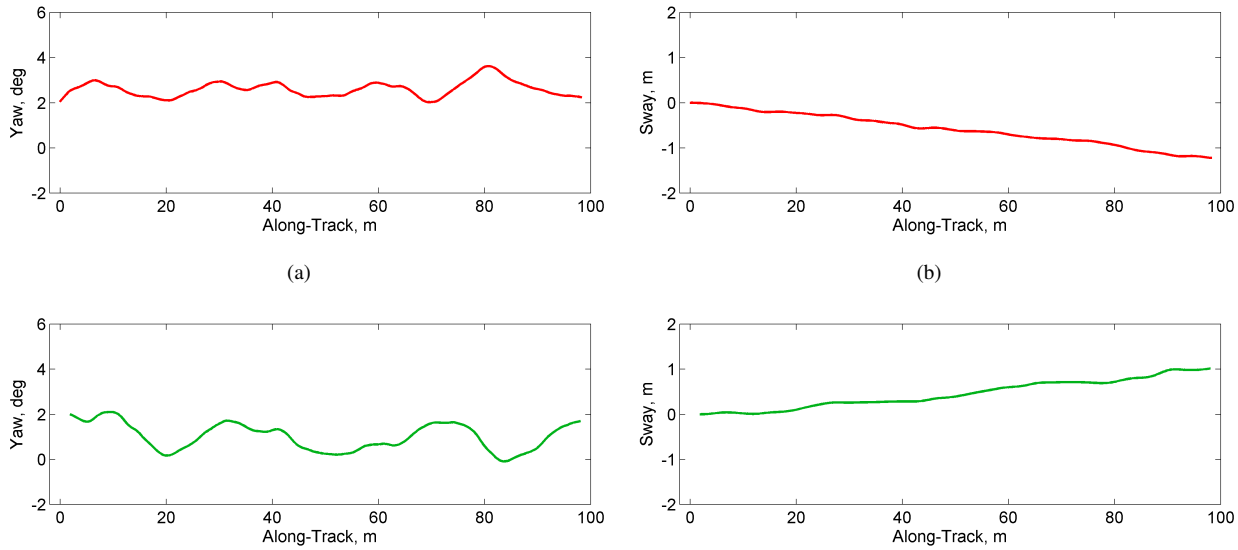

(a) (b) (c) (d)

Fig. 7. Independently estimated paths of the first (a,b) and second (c,d) passes using conventional RPC micro-navigation.

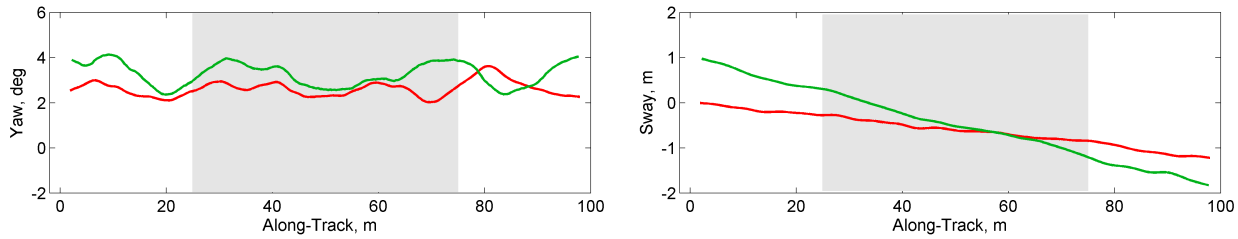

(a) (b)

Fig. 8. Mutually estimated paths of the first (red) and second (green) passes in a common coordinate frame using repeat-pass RPC micro-navigation. The gray region indicates the along-track portions corresponding to the SAS images.

E. Synthetic aperture sonar (SAS) imaging and repeat-pass interferometry

Co-registered SAS images can be generated directly from the matched-filtered echo data using the repeat-pass RPC micro-navigation estimates. Using back-projection, the co-registered image from the ith pass in the slant-range plane of the common coordinate system is given by the coherent sum over pings p and array elements n, i.e.,

$$I_i(\mathbf{x}) = \sum_{p=0}^{P-1} \sum_{n=0}^{N-1} d_p^{(i)} \left(\frac{2}{c} r_{p,n}^{(i)}(\mathbf{x}), u \right) \tag{36}$$

where $\mathbf{x} = (x, y)$ are the locations of the image pixels,

$$r_{p,n}^{(i)}(\mathbf{x}) = \left| \mathbf{x} - \mathbf{u}_{p,n}^{(i)} \right| \tag{37}$$

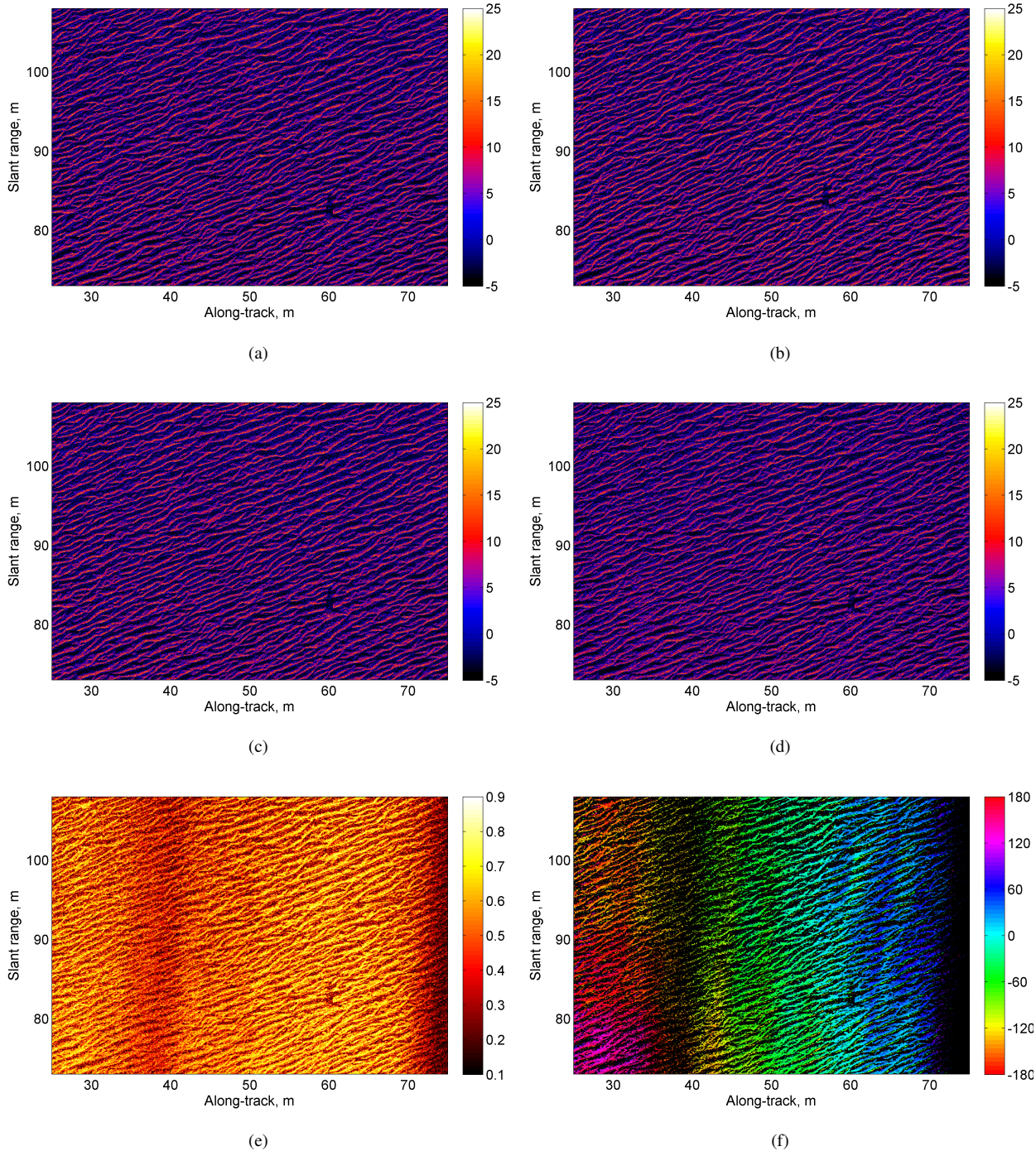

Fig. 9. SAS images from the (a) first pass and (b) second pass focused independently using RPC micro-navigation; SAS images from the (c) first and (d) second pass focused and co-registered using repeat-pass RPC micro-navigation; (e) image coherence between first and second passes; (f) interferometric phase.

are the one-way distances from the phase centers to the pixels, and

$$\mathbf{u}_{p,n}^{(i)} = \hat{\mathbf{x}}_p^{(i)} + \begin{pmatrix} \cos\hat{\theta}_p^{(i)} \\ \sin\hat{\theta}_p^{(i)} \end{pmatrix} u \tag{38}$$

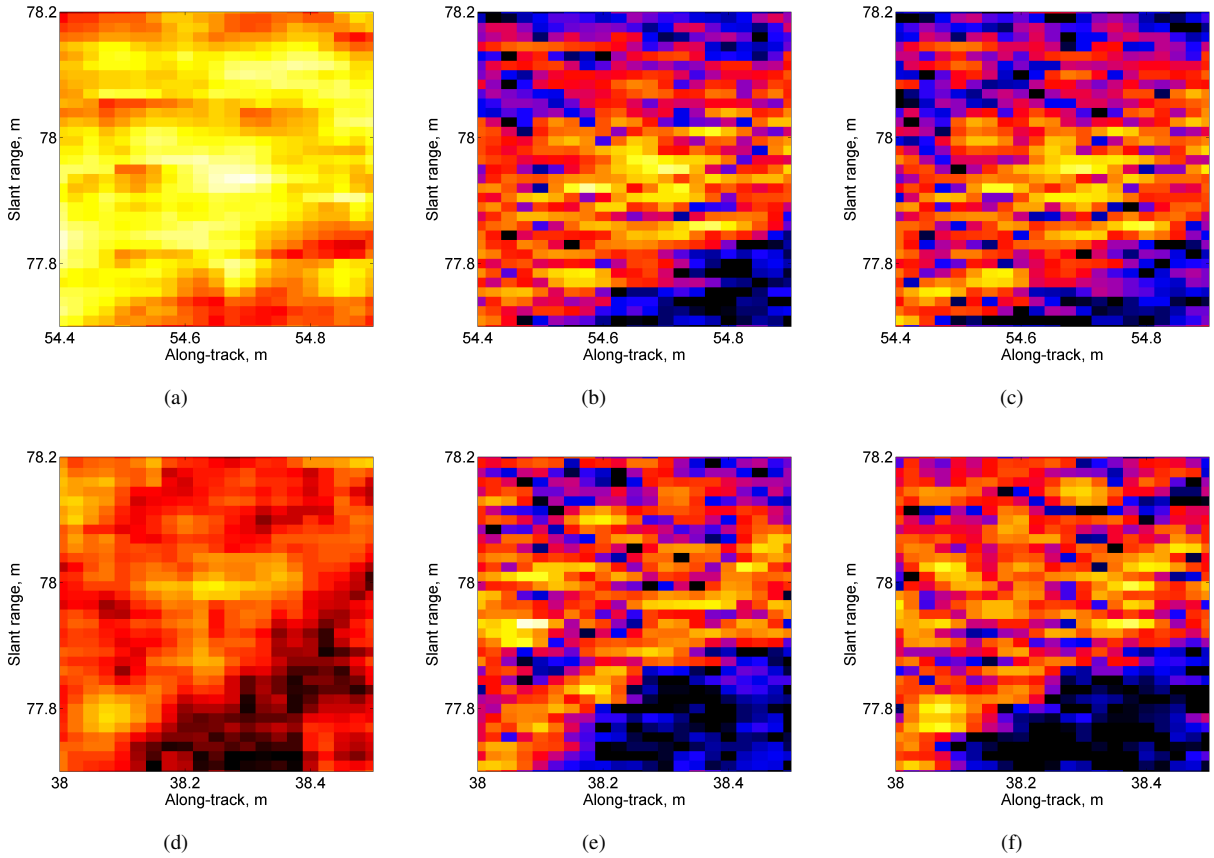

Fig. 10. Zoomed regions of (a) high image coherence of approximately 0.7-0.9 and (d) low image coherence of approximately 0.5-0.7; (b,e) are the corresponding image regions from the first pass and (c,f) from the second pass.

are the phase center locations. Note that (36) is a vast over-simplification of SAS imaging and it ignores many of the practicalities, such as: interpolation of the data from redundant phase centers, interpolation of the slant-range micro-navigation estimates, a Jacobian term for mapping between along-track positions and azimuth angles, and spatio-temporal filtering due to the beam patterns and signal bandwidth. It is presented only for the purpose of illustrating how the micro-navigation estimates $\hat{\theta}_p^{(i)}$ and $\hat{\mathbf{x}}_p^{(i)}$, obtained from (26) and (34), are incorporated into the imaging procedure.

An interferogram can be formed between co-registered images from repeated passes, i.e.,

$$\Lambda\left(\mathbf{x}\right) = \frac{\mathrm{E}\left\{I_1\left(\mathbf{x}\right) I_2^*\left(\mathbf{x}\right)\right\}}{\sqrt{\mathrm{E}\left\{\left|I_1\left(\mathbf{x}\right)\right|^2\right\}\mathrm{E}\left\{\left|I_2\left(\mathbf{x}\right)\right|^2\right\}}}. \tag{39}$$

In practice, the ensemble averages in (39) cannot be computed and must be approximated using sample averages, e.g., over a region of $L \times L$ pixels. The interferogram provides a measure of the coherence $\left|\Lambda\left(\mathbf{x}\right)\right|$ and phase difference $\angle\Lambda\left(\mathbf{x}\right)$ between corresponding regions in each of the images. The image coherence quantifies the similarity of the acoustic scattering represented within each region and its magnitude can vary from a minimum of $1/L$ (uncorrelated

noise samples) to 1 (exactly the same) [23]. Assuming that the co-registration has been performed correctly, the change in scattering properties represented by coherence loss and phase differences can be attributed to a combination of three factors: different geometrical views, temporal changes in the seafloor or medium, and ambient noise.

III. Experimental results

The repeat-pass RPC micro-navigation algorithm is demonstrated on data collected using the synthetic aperture sonar on the MUSCLE autonomous underwater vehicle (AUV) of the NATO Center for Maritime Research and Experimentation, shown in Figure 3. The SAS has a center frequency of $300\ \mathrm{kHz}$ and a bandwidth of $60\ \mathrm{kHz}$ [25]; the receiver array is comprised of 36 elements with a spacing of $3.33\ \mathrm{cm}$ and has a total length of $1.2\ \mathrm{m}$. The navigation system on the MUSCLE is comprised of an inertial measurement unit, Doppler velocity log, and global positioning system sensor. The data were collected during the MANEX '14 trial in the Ligurian Sea, near the coast of Framura, Italy. The seabed in the area is at a depth of approximately $20\ \mathrm{m}$; it is sandy and was rippled at the time. Repeated passes were made by the AUV at a speed of $4\ \mathrm{m/s}$ and an altitude of approximately $10\ \mathrm{m}$ above the seafloor. The SAS was operated at a ping rate of $4\ \mathrm{pings/s}$, resulting in approximately 4 overlapping phase centers between subsequent pings within the same pass. Multiple passes were made with $1\ \mathrm{deg}$ increments in heading prescribed between each successive pass to provide a relative sway and to ensure a crossing point. A time of 16 min, 30 sec elapsed between each pass. The tracks of the first two passes as measured by the INS and DVL are shown in Figure 4.

An interval of 256 pings centered roughly on the crossing point of the passes was considered. The pings were aligned as described in Section II-D, but correlations were only observed for passes that were separated by $1\ \mathrm{deg}$ and $2\ \mathrm{deg}$ increments. Correlations were not observed for greater separations due to the $2.5\ \mathrm{deg}$ half-beamwidth of the sonar. Between the first and second passes (separated by $1\ \mathrm{deg}$), an offset of between 3 and 5 pings was observed relative to the start of each pass, as is shown in Figure 6a. Since the tracks were planned with identical lengths and vehicle speeds, these variations in the ping offset are thought to be due to the influence of the underwater current. This is supported by observations of a greater variation in offsets for the passes separated by $2\ \mathrm{deg}$. Unless otherwise stated, the following results are from the first and second passes (separated by $1\ \mathrm{deg}$).

The conventional RPC micro-navigation algorithm was applied to each pass independently over $5\ \mathrm{m}$ slant-range windows from $70\ \mathrm{m}$ to $110\ \mathrm{m}$. The intra-pass ping-to-ping coherence at a slant-range of $85\ \mathrm{m}$ is shown in Figure 5a with similar values being observed over the other windows. The coherence varies between approximately 0.7 and 0.9 along the path. The resulting intra-pass sway and surge rate estimates were integrated to produce the estimated paths shown in Figure 7b and Figure 7d for passes 1 and 2, respectively. These were used together with the INS estimates of the yaw shown in Figure 7a and Figure 7c to generate two focused SAS images of the seafloor.

The independently focused SAS images from the first and second passes are shown in Figure 9a and Figure 9b respectively. Overall, the images appear very similar, both revealing a rippled seafloor with a single proud object. However, an obvious difference is the along-track offset of approximately $3.5\ \mathrm{m}$ and the slant-range offset of approximately $2\ \mathrm{m}$. These are caused by the $1\ \mathrm{deg}$ rotation between the images induced by the relative heading

difference between passes and the 3-5 ping navigation offset.

The repeat-pass RPC algorithm was applied to the two passes mutually over the same slant-range windows as before. The coherence values are shown in Figure 5a for the directly corresponding inter-pass ping pairs denoted in Section II-B by $\cdot_{p,p}^{(12)}$. The number of overlapping phase centers in the direct inter-pass pairs varied between $N/2 = 18$ (near a ping offset transition) and $N = 36$. Again, the results are shown at a slant-range of $85\ \mathrm{m}$ with similar results being observed at the other ranges. Furthermore, the other inter-pass ping pair combinations, denoted by $\cdot_{p-1,p}^{(12)}$ and $\cdot_{p-1,p}^{(21)}$, yielded similar values. Obviously, the intra-pass values, $\cdot_{p-1,p}^{(11)}$ and $\cdot_{p-1,p}^{(22)}$, are identical to those computed previously. The inter-pass coherence varied between approximately 0.2 and 0.8. Comparison with the intra-pass coherence from the conventional RPC micro-navigation shows that the inter-pass coherence attains comparable values to the intra-pass coherence for regions of the repeated passes nearby the crossing point. This indicates that decorrelation due to temporal changes of the seafloor is low over the period of time between passes. Away from the crossing point, the decorrelation can be attributed to the geometrical effects of an increasing baseline and footprint misalignment at greater separations. For comparison, the intra and inter-pass coherence values are shown in Figure 5b for the first and third passes (separated by $2\ \mathrm{deg}$). Here, a maximum coherence of only 0.6 is attained. This reduction can be attributed mostly to the footprint misalignment caused by the nominal difference in look directions and the limited sonar beamwidth. The minimum coherence of 0.1 in this case is consistent with the value expected for uncorrelated noise observed over the bandwidth of $60\ \mathrm{kHz}$ and the selected time window of $6.67\ \mathrm{ms}$ ($5\ \mathrm{m}$ slant range) [23].

The inter-pass surge, sway, and yaw estimates are shown in Figure 6, where they are compared with the measurements from the navigation hardware. The yaw is in very good agreement with the navigation hardware. The overall trends in the surge and sway are similar. However, there is a bulk offset between the measurements and micro-navigation estimates of approximately 0.5 - $1\ \mathrm{m}$. Presumably this is due to INS and DVL measurement drift [26]. Moreover, the micro-navigation is shown to provide a much smoother estimate. Using the WLS solution, the paths of the repeated passes were estimated mutually from the intra and inter-pass rate estimates in a common coordinate frame and these are shown in Figure 8.

The estimated paths of the repeated passes were used to generate co-registered SAS images, which are shown in Figure 9c and Figure 9d. To evaluate the co-registration, an interferogram was formed using an averaging window of 5×5 pixels. The resulting coherence map is shown in Figure 9e and the phase difference map is shown in Figure 9f. Note that the phase differences with coherence less than 0.2 have been masked to suppress the random phase estimates in the shadow zones. An image coherence of up to 0.9 is achieved over most of the image. Obviously, the coherence reduces to a minimum in the shadowed troughs of the seafloor ripples where the acoustic back-scattering strength is low. However, there are also two bands of low coherence with a maximum of only 0.7 at along-track positions of $35 - 40\ \mathrm{m}$ and $70 - 75\ \mathrm{m}$. A comparison is made in Figure 10 between two enlarged areas of seafloor in regions of high and low image coherence. Here, it can be observed that the speckle patterns are indeed similar where the coherence values are high and dissimilar where they are low. The bands of low coherence are due to footprint misalignment caused by relative yaw between the passes, which becomes significant when the angles

are on the order of the sonar half-beamwidth or greater (i.e., $2.5\ \mathrm{deg}$ for the MUSCLE). Correspondence between the bands and the larger yaw values can be observed in Figure 8a. Although the prescribed heading difference was $1\ \mathrm{deg}$, in practice, the efforts of the AUV to maintain a straight path cause variations from $0\ \mathrm{deg}$ to $2\ \mathrm{deg}$.

The phase difference map exhibits a continuous and gradual variation over the scene. Furthermore, the variations are less than one wavelength and no phase wrapping is observed. This is consistent with our expectations of zero (or near zero) phase difference imposed by the algorithm.

IV. Conclusions and Future Work

Repeat-pass RPC micro-navigation is a new algorithm for improved repeat-pass SAS data co-registration, imaging, and interferometry. It is a generalization of RPC micro-navigation that exploits the temporal (as well as spatial) coherence of scattering from the seafloor, providing precision estimates of repeated passes in a common coordinate frame. The algorithm has been demonstrated using data collected at sea by the $300\ \mathrm{kHz}$ SAS of the CMRE MUSCLE AUV.

Micro-navigation estimates were made and then used to generate co-registered SAS images from repeated passes with a nominal heading difference of $1\ \mathrm{deg}$ and separated by a time period of approximately 15 min. The precision of the image registration was evidenced by the interferometric map, where coherence values of 0.9 and sub-wavelength phase differences were achieved over most of the observed parts of the scene. Furthermore, these interferometric results show that coherent change detection is feasible using the MUSCLE in the region of the Ligurian Sea where the MANEX'14 trial was conducted, at least over time scales of tens of minutes. Further data collection is necessary to quantify the long-term temporal coherence of the seafloor in this area.

The dominant cause of inter-pass decorrelation (over time scales of tens of minutes) was found to be caused by relative differences in the geometry between passes. In particular, relative yaw had a significant effect. For the MUSCLE, a heading difference of less than $2\ \mathrm{deg}$ is desired due to the half-beamwidth limit of $2.5\ \mathrm{deg}$.

In future repeat-pass missions, considerations should be made within the vehicle's control strategy to establish a compromise between minimizing the rotational yaw errors in addition to the translational path errors. In current practice, this compromise is not generally considered. Other areas for future investigation and development include: 1) modeling and measuring the operational constraints imposed by the limited temporal and spatial coherence of the seafloor scattering; 2) quantifying the improvements in focusing and co-registration quality offered by the method; and 3) further developments to preserve bathymetry-induced phase differences from an interferometric baseline for enhanced seafloor bathymetric mapping.

Acknowledgment

This work was funded by the NATO Allied Command Transformation. The authors would like to thank the CMRE engineering department and the crew of the NRV Alliance for their support in collecting the experimental data during the MANEX '14 trial. Dr. Hunter is grateful to CMRE for hosting him during the summer of 2014.

REFERENCES

[1] M. P. Hayes and P. T. Gough, "Synthetic aperture sonar: a review of current status," *IEEE J. Ocean. Eng.*, vol. 34, no. 3, pp. 207–224, Jul. 2009.

[2] ——, "Broad-band synthetic aperture sonar," *IEEE J. Ocean. Eng.*, vol. 17, no. 1, pp. 80–94, Jan. 1992.

[3] W. G. Carrara, R. S. Goodman, and R. M. Majewski, *Spotlight Synthetic Aperture Radar: Signal Processing Algorithms*. Artech House, 1995.

[4] D. A. Cook and D. C. Brown, "Analysis of phase error effects on stripmap SAS," *IEEE J. Ocean. Eng.*, vol. 34, no. 3, pp. 207–224, Jul. 2009.

[5] M. A. Pinto, A. Bellettini, S. Fioravanti, S. Chapman, D. R. Bugler, Y. Perrot, and A. Hétet, "Experimental investigations into high resolution sonar systems," in *Proceedings of IEEE/MTS Oceans*, Seattle, WA, Sep. 1999.

[6] R. E. Hansen, T. O. Sæbø, K. Gade, and S. Chapman, "Signal processing for AUV based interferometric synthetic aperture sonar," in *Proceedings of IEEE/MTS Oceans*, San Diego, CA, Sep. 2003.

[7] R. S. Raven, "Electronic stabilization for displaced phase center systems," Patent US 4 244 036 A, Jan., 1981.

[8] R. W. Sheriff, "Synthetic aperture beamforming with automatic phase compensation for high frequency sonars," in *Proceedings of the Symposium on Autonomous Underwater Vehicle Technology*, Washington DC, USA, Jun. 1992.

[9] D. Billon and F. Fohanno, "Theoretical performance and experimental results for synthetic aperture sonar self-calibration," in *Proceedings of IEEE Oceans*, Nice, France, Sep. 1998.

[10] A. Bellettini and M. A. Pinto, "Theoretical accuracy of synthetic aperture sonar micronavigation using a displaced phase-center antenna," *IEEE J. Ocean. Eng.*, vol. 27, no. 4, pp. 780–789, Oct. 2002.

[11] A. P. Lyons and D. C. Brown, "The impact of the temporal variability of sea floor roughness on synthetic aperture sonar repeatpass interferometry," *IEEE J. Ocean. Eng.*, vol. 38, no. 1, pp. 91–97, Jan. 2013.

[12] T. O. Sæbø, S. A. V. Synnes, and R. E. Hansen, "Wideband interferometry in synthetic aperture sonar," *IEEE Trans. Geosci. Remote Sens.*, vol. 51, no. 8, pp. 4450–4459, Aug. 2013.

[13] M. A. Richards, "A beginners guide to interferometric SAR concepts and signal processing," *IEEE Aerosp. Electron. Syst. Mag.*, vol. 22, no. 9, pp. 5–29, Sep. 2007.

[14] D. D. Sternlicht, J. K. Harbaugh, and M. A. Nelson, "Experiments in coherent change detection for synthetic aperture sonar," in *Proceedings of IEEE/MTS Oceans*, Biloxi MS, USA, Oct. 2009.

[15] T. G-Michael and J. D. Tucker, "Canonical correlation analysis for coherent change detection in synthetic aperture sonar imagery," in *Proceedings of the International Conference on SAR and SAS*, Lerici, Italy, Sep. 2010.

[16] T. O. Sæbø, R. E. Hansen, H. J. Callow, and S. A. V. Synnes, "Coregistration of synthetic aperture sonar images from repeated passes," in *Proceedings of the European Conference on Underwater Acoustics (ECUA)*, Istanbul, Turkey, Jul. 2010.

[17] T. G-Michael, B. Marchand, J. D. Tucker, D. D. Sternlicht, and T. M. Marston, "Automated change detection for synthetic aperture sonar," in *Proceedings of SPIE*, May 2014.

[18] S. A. V. Synnes, H. J. Callow, R. E. Hansen, and T. O. Sæbø, "Multipass coherent processing on synthetic aperture sonar data," in *Proceedings of the European Conference on Underwater Acoustics (ECUA)*, Istanbul, Turkey, Jul. 2010.

[19] D. A. Cook, "Synthetic aperture sonar motion estimation and compensation," Master's thesis, School of Electrical and Computer Engineering, Georgia Institute of Technology, Atlanta GA, USA, May 2007.

[20] S. Banks, "Studies in high resolution synthetic aperture sonar," Ph.D. dissertation, University College London, London, UK, 2002.

[21] J. Groen, "Adaptive motion compensation in sonar array processing," Ph.D. dissertation, Technische Universiteit Delft, Delft, The Netherlands, Jun. 2006.

[22] J. Groen, H. Schmaljohann, W. Jans, and U. Hölscher-Höbing, "Comparison of fusion approaches for the displaced phase centre antenna method," in *Proceedings of the 2nd International Conference and Exhibition on Underwater Acoustics*, Rhodes, Greece, Jun. 2014.

[23] G. C. Carter, C. H. Knapp, and A. H. Nuttall, "Statistics of the estimate of the magnitude-coherence function," *IEEE Trans. Audio Electroacoust.*, vol. 21, no. 4, pp. 388–389, Aug. 1973.

[24] R. Penrose, "A generalized inverse for matrices," *Mathematical Proceedings of the Cambridge Philosophical Society*, vol. 51, no. 3, pp. 406–413, 1955.

[25] A. Bellettini and M. A. Pinto, "Design and experimental results of a 300-kHz synthetic aperture sonar optimized for shallow-water operations," *IEEE J. Ocean. Eng.*, vol. 34, no. 3, pp. 285–293, Jul. 2009.

[26] R. Panish and M. Taylor, "Achieving high navigation accuracy using inertial navigation systems in autonomous underwater vehicles," in *Proceedings of IEEE/MTS Oceans*, Santander, Spain, Jun. 2011.

Alan J. Hunter was born in Christchurch, New Zealand, in 1978. He received the B.E.(Hons) and Ph.D. degrees in electrical and electronic engineering from the University of Canterbury (NZ) in 2001 and 2006, respectively. From 2007 to 2010, he was a research associate at the University of Bristol, England and from 2010 to 2014 he was a defense scientist at TNO (Netherlands Organisation for Applied Scientific Research), The Netherlands. Since 2014, Dr. Hunter has been a lecturer in the Faculty of Engineering and Design at the University of Bath, England. Dr. Hunter's research interests are in underwater acoustics, sonar imaging of the seafloor, and autonomous underwater systems.

Samantha Dugelay was born in London, England in 1969. She received a B.Sc. and M.Sc. in Mathematics from the Université de Bretagne Occidentale, Brest, France in 1991 and 1993 respectively, a Diplôme d'Études Approfondies in Statistical and Stochastic Modelling in 1994 and a Ph.D. degree in Mathematics in 1997 both from the Université de Paris Sud, Orsay, France. From 1997 to 2000 she worked as a research associate at University College London and then the University of Bath, England. She joined QinetiQ in 2000 as a Senior Scientist and then transferred to Dstl in 2006 as a technical lead for MCM sensor requirements and MCM automatic target recognition. Since 2013, Samantha has been working at the Centre for Maritime Research and Experimentation in La Spezia, Italy as the project leader on Autonomous Mine Search. Dr Dugelay's interests lie in autonomous maritime vehicles, underwater acoustics and sonar data processing.

Warren L. J. Fox received the B.S., M.S., and Ph.D. degrees in electrical engineering from the University of Washington, Seattle, WA. Currently, he is a Senior Principal Research Scientist at the Applied Physics Laboratory, University of Washington (APL-UW). Previously, he was a Principal Scientist and Program Manager for Autonomous Naval Mine Countermeasures at the NATO Science and Technology Organizations Centre for Maritime Research and Experimentation (CMRE) in La Spezia, Italy. Other previous positions were Director of R&D and Navy Systems for BlueView Technologies, Senior Electrical Engineer at APL-UW, and Scientist at the NATO SACLANT Undersea Research Centre. His technical expertise is in the areas of statistical signal and image processing, underwater acoustics, sonar systems, robotics, and autonomy.